Journal of Materials Chemistry C

ROYAL SOCIETY OF CHEMISTRY

PAPER

View Article Online
View Journal | View Issue

Published on 27 May 2021. Downloaded by HeFei University of Technology on 8/4/2021 2:17:17 AM.

Check for updates

Cite this: *J. Mater. Chem. C*, 2021, **9**, 8855

Distinguishing wavelength using two parallelly stacking graphene/thin Si/graphene heterojunctions†

Lin-Bao Luo, *[a] Ting Fang,[a] Chao Xie,[b] Li Wang,*[a] Di Wu [c] and Feng-Xia Liang*[d]

Received 22nd April 2021,
Accepted 20th May 2021

DOI: 10.1039/d1tc01871j

rsc.li/materials-c

In this work, we have developed a wavelength sensor that is capable of distinguishing illumination with wavelengths ranging from ultraviolet (UV) to near infrared (NIR). The as-proposed wavelength sensor is geometrically composed of two parallelly stacking graphene (Gr)/thin Si/Gr heterojunction devices, which are identical in device structures, but can display completely different optical properties in terms of distribution of photo-absorption and photo-generation rates under various light illuminations, according to theoretical simulation. Such a discrepancy in optical properties due to a wavelength dependent absorption coefficient and the relatively thin Si wafer gives rise to completely different photocurrent evolution for varied wavelengths of illumination. The relationship between the photocurrent ratio of devices, the wavelength and intensity of incident light can be numerically described by an equation, through which the wavelength in the range from 265 to 1050 nm can be accurately determined. Notably, the average root-mean-square error of this wavelength sensor is about 2.30 nm, with a relative error as low as ±1.5%, which is much better than other wavelength detectors previously reported. These results suggest that the present wavelength sensor may find potential application for future optoelectronic systems.

Introduction

Wavelength sensors which are capable of detecting a wide range of wavelengths from the ultraviolet (UV)-visible to the near infrared (NIR) region have found application in a wide range of fields including artificial intelligence systems, imaging sensors, safety protection, optical communication and autonomous vehicles.[1–6] For example, by controlling the absorption of red, green, and blue illumination using a microcavity structure, a wavelength detector has been achieved for real image reproduction, which is of great significance to vision systems.[7] In addition, a monitoring system composed of a wavelength detector can accurately monitor the target object by detecting the movement of the color and position of the object, which can further optimize the precise positioning and tracking of the security system.[8]

Benefiting from the rapid advance of optoelectronic devices, many sorts of wavelength detectors with different device geometries for reliable detection of wavelength have been developed in the past decades. The first and most representative technique is to use a color filter array (CFA) to detect the relative share of red, green and blue (RGB), respectively, and then convert the RGB value to the wavelength of the incident light by referring to the CIE (International Commission on Illumination) 1931 color space. This technique is characterized by using a filter and the detection range of 380–700 nm.[9–14] Another strategy for wavelength detection mainly relies on transverse field detectors (TFDs) that are able to discriminate photons with various wavelengths in the range of 400–900 nm. Typically, this special approach mainly implies an electric field that is able to collect a photo-carrier within the active layer of the device.[15–18] By employing BDJ (buried double p–n junction) or BTJ (buried triple p–n junction) structures, the wavelength of incident light in the 400–950 nm range can also be determined by the optical admittance of a medium dominated vertical stack strategy, with a wavelength detection error of about 5–10 nm.[19–21] In spite of the above tremendous achievements, it is undeniable

[a] *School of Electronic Science and Applied Physics, Hefei University of Technology, Hefei, Anhui 230009, P. R. China. E-mail: luolb@hfut.edu.cn, wlhgd@hfut.edu.cn*
[b] *School of Electronics and Information Engineering, Anhui University, Hefei, Anhui 230601, P. R. China*
[c] *School of Physics and Engineering and Key Laboratory of Material Physics of Ministry of Education, Zhengzhou University, Zhengzhou, Henan 450052, P. R. China*
[d] *School of Materials Sciences and Engineering, Hefei University of Technology, Hefei, 230009, P. R. China. E-mail: fxliang@hfut.edu.cn*

† Electronic supplementary information (ESI) available: Fig. S1–S5. See DOI: 10.1039/d1tc01871j

Published on 27 May 2021. Downloaded by HeFei University of Technology on 8/4/2021 2:17:17 AM.

that these techniques have their own shortcomings: (1) relatively complicated device geometries. The fabrication of these devices often involves the integration of a number of optical components and photodetectors with different photosensitive materials, which inevitably leads to complicated device fabrication processes and high fabrication costs.[22–25] (2) Relatively narrow detection range. To our knowledge, the majority of the above wavelength detectors have been mainly developed for detecting visible light bands. While there are a few reports that claim the detection of wavelength in the range of near infrared, it is however at the cost of detection resolution, which is far from satisfactory, from the perspective of practical application.[26–28]

In light of the above, we herein report on a new concept of wavelength detectors which are able to distinguish the spectrum with a wavelength ranging from 250 to 1050 nm. The as-proposed device is geometrically composed of two horizontally stacking graphene (Gr)/20 μm Si/Gr heterojunction photodetectors. It is revealed that when shined by light illumination with different wavelengths, the two heterojunction devices with identical geometry will exhibit different photo-absorption and photo-generation rate distribution, owing to the thinness of the Si wafer and wavelength dependent absorption coefficient. Such a unique optical property leads to a monotonic increase in the corresponding photocurrent ratio with increasing wavelength. In fact, the relationship between wavelength and photocurrent ratio can be described by an equation, *via* which the wavelength of the incident light can be determined. Further device analysis finds that the present wavelength sensor can readily detect a wavelength in the range from 250–1050 nm, with an average root-mean-square error of around 2.30 nm and a relative error as low as ±1.5%, which is much better than previously reported devices.

Experimental

Device fabrication and analysis

20 μm thick phosphorus doped n-type (100) single-crystalline silicon (diameter: 2 inches, doping concentration of 10^{15} cm^{-3}, resistivity: 1–10 Ω cm, double side polished) was purchased from the University Wafer INC. The Gr used in this work was synthesized by a conventional chemical vapor deposition method, in which 50 μm Cu foils and a mixed gas of CH_4 and H_2 were used as the catalytic substrate and precursor, respectively. The detailed fabrication process for the growth of graphene can be found in our previous work.[29] To assemble the Gr-silicon heterojunction device, the above CVD single-layer Gr supported by polymethyl methacrylate (PMMA) was transferred onto the surface of an n-type silicon film, which was cleaned with alcohol and acetone and placed on a glass substrate in advance. Afterwards, photolithography technique was used to define the pattern on the as-assembled sample, followed by an oxygen plasma treatment to produce a patterned Gr film with an interdigitated structure. Finally, by assembling two identical Gr/thin Si heterojunctions onto a PCB substrate, a color sensor that is able to discriminate different wavelengths was obtained. The quality of the Gr layer was characterized using a Raman spectrometer (Horiba Jobin Yvon, LabRAM HR800). What is more, the cross section of the thin Si was studied by scanning electron microscopy (SEM, KYKY-6900).

Theoretical simulation

The photoelectric characteristics of both Gr-thin Si heterojunction and color sensor were investigated using an *I–V* semiconductor characterization system (4200-SCS, Keithley Co. Ltd) attached with a monochromator (SP2150, Princeton Co.). In addition, some light emitting diode light sources with specific wavelengths (*e.g.*, 265 nm, 450nm, 530 nm, 660 nm, 730 nm, 810 nm, 970 nm, 1050 nm, and 1300 nm) were also used in this study (Thorlabs). Note that the power intensity of all incident light was calibrated using a power-meter (Thorlabs GmbH., PM 100D), before optoelectronic analysis. The simulation was carried out using the Synopsys Sentaurus TCAD to study the photo-absorption rate and photo-generation rate. For convenience, the photo-absorption rate and photo-generation rate of two silicon wafers were considered in the TCAD simulation. A grid point number of 31810 was chosen as a compromise between computing time and precision, since finer meshes have been tried without obvious changes. During calculation, a beam of light with an intensity of 1 mW cm^{-2} shines perpendicularly to the heterojunction detector.

Results and discussion

The proof-of-concept wavelength sensor is composed of two Gr/thin Si/Gr heterojunctions that are assembled in a parallelly stacking manner (Fig. 1(a)). Fig. S1 (ESI†) shows a flow-chart process for fabricating a single Gr/thin Si/Gr photodetector. Basically, a Gr layer that is pre-supported by poly (methylmethacrylate) (PMMA) was firstly transferred onto the surface of an n-type thin Si wafer, whose thickness is determined to be about 20 μm from the scanning electron microscopy image (Fig. 1(b)). The as-obtained sample was then treated by acetone to remove the PMMA, followed by reactive ion etching (RIE) to form

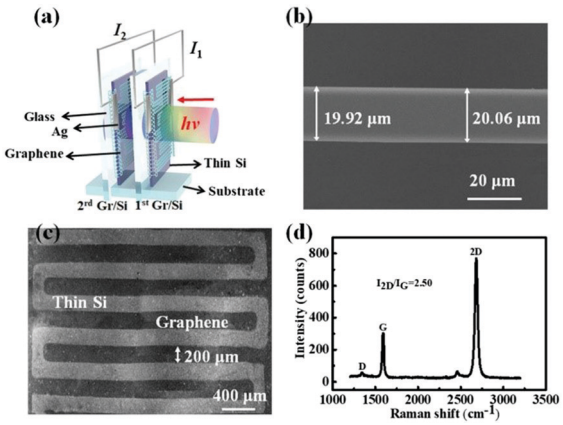

Fig. 1 (a) The device geometry of the wavelength sensor which is composed of two horizontally stacking Gr/thin Si/Gr heterojunctions. (b) The cross-section SEM image of the thin Si wafer. (c) The FESEM image of the Gr/thin Si/Gr devices. (d) Raman spectrum of the Gr layer.

 This journal is © The Royal Society of Chemistry 2021

Published on 27 May 2021. Downloaded by HeFei University of Technology on 8/4/2021 2:17:17 AM.

interdigitated electrodes, with a gap of 200 μm (Fig. 1(c)). For convenience, the two identical vertically standing heterojunction photodetectors were then fixed onto a glass substrate. The Gr used in this study is composed of single layer Gr with very few defects, as revealed by the Raman study in (Fig. 1(d)). Such single layer Gr is very important for the realization of a wavelength sensor in that it only absorbs 2.5–7.5% of light in the range from 250 to 1100 nm, according to previous studies.[30,31] In addition, the relatively low sheet resistance (around 260 Ohm sq^{-1}) can greatly facilitate the transport of carriers during the wavelength sensing process.[32]

From the viewpoint of device geometry, the present Gr/thin Si/Gr heterojunction device is quite similar to other Gr or two dimensional material-based heterojunction photodetectors, which have been extensively studied in the past decade.[33–35] Nonetheless, it exhibits rather different optical and optoelectronic properties because of the relatively small thickness of the Si wafer. Fig. 2 shows the simulated distribution of both photo-absorption rate and photo-generation rate at different wavelengths of illumination which are obtained by using Synopsys Sentaurus Technology Computer Aided Design (TCAD).[36,37] Since the Gr layer absorbs very limited light in the UV to NIR light region and the glass between the two parallel photodetectors is nearly transparent in the same region (Fig. S2, ESI†), only two planar thin Si wafers with a thickness of 20 μm were taken into consideration during the TCAD simulation. Fig. 2(a) shows the photo-absorption rate of both heterojunction photodetectors when shined on by different wavelengths of illumination. One can easily find that with the increase in light wavelength, the corresponding penetration depth (the physical depth that can absorb incident light) will increase due to the reduced absorption coefficient at relatively longer wavelengths (Fig. S3, ESI†).[38] On this account, the absorption edge of 20 μm Si was found to shift from 1000 nm (for bulk Si) to 800 nm (Fig. S4, ESI†). Notably, for illumination of 250 and 300 nm light, the photo-absorption rate at the first device is as high as 10^{23} cm^{-3} at the superficial surface of the thin Si (only several tens of nm from the surface, Fig. 2(b)), but is close to zero for the whole thickness of the second device (Fig. 2(c)). However, with the gradual increase in wavelength, the penetration depth will be extended to the entire thickness of the first device and even to the second device when the wavelength is larger than 950 nm. A similar finding was also found in the evolution of photo-generation rate as a function of different wavelengths (Fig. 2(d–f)). In fact, the above optical properties of both devices were also verified by Fig. 2(g) and (h), which quantitatively plot the distribution of the photo-absorption rate of both devices when illuminated by the incident light with wavelengths ranging from 250 to 1200 nm. It is clear that the short wavelength light is mainly absorbed at the surface of the first device, while the absorption of light with a long wavelength is not only achieved by the first device, but also by the second device, in line with the above mapping result. These results suggest that the incident light with a short wavelength can cause a significant difference in photocurrent for both devices because of their sharp discrepancy in light absorption. In contrast, when the light is replaced with a longer wavelength, owing to comparable photo-absorption, very close distribution of photo-absorption and photo-generation rates for both devices will be observed.

Thanks to the wavelength dependent absorption coefficient of the Si, the photo-absorption rates are different throughout the thickness, as illustrated in Fig. 3(a). Thereby, the overall light absorption of the whole device can be calculated by the following integral formula:

$$A = S * \lim_{i \to 0} \sum_{i}^{n} f(\xi_i)\Delta x_i = s * \int_{0}^{0.0002} f(x) * dx \qquad (1)$$

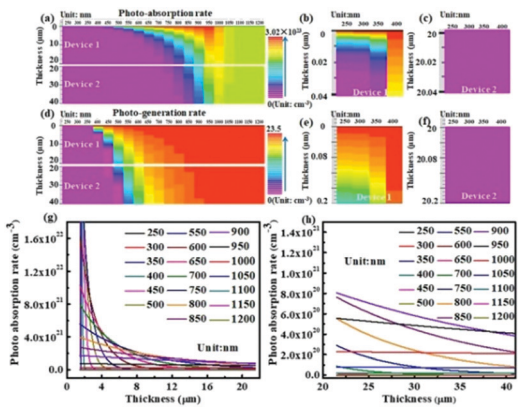

Fig. 2 (a) Contour mapping of the photo-absorption rate as a function of different wavelengths for two Gr/thin Si/Gr heterojunction devices. The magnified mapping of the photo-absorption rate at the surface of the first (b) and second (c) Gr/thin Si/Gr devices under illumination of short wavelength. (d) Contour mapping of the photo-generation rate as a function of different incident light wavelength for two Gr/thin Si/Gr devices. The magnified mapping of the photo-generation rate at the surface of the first (e) and second (f) Gr/thin Si/Gr devices under illumination of very short wavelength. (g) Photo-absorption rate of 250–1200 nm light in the first Gr/thin Si/Gr heterojunction detector. (h) Photo-absorption rate of 250–1200 nm light in the second Gr/thin Si/Gr heterojunction detector.

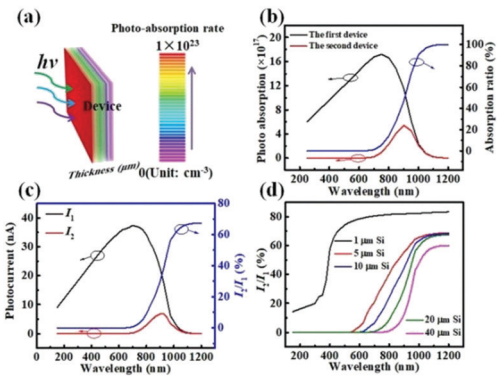

Fig. 3 (a) Schematic diagram of the entire device absorption. (b) Photo-absorption of each device and absorption ratio at different wavelengths. (c) Simulated photocurrent of each device and the corresponding photo-current ratio of the two Gr/thin Si/Gr devices at different wavelengths. (d) Simulated photocurrent ratio of the two Gr/thin Si/Gr heterojunction devices at various wavelengths with different thicknesses.

Published on 27 May 2021. Downloaded by HeFei University of Technology on 8/4/2021 2:17:17 AM.

where A is the overall absorption, S is the device area, x is the thickness of the Si wafer, and $f(x)$ is the function of the photo-absorption rate. Fig. 3(b) compares the theoretical photo-absorption of both heterojunction photodetectors in the range from 250 to 1200 nm. It is obvious that the two devices exhibit a remarkable difference, not only in absorption intensity but also in the location of maximum absorption. The strongest absorption for the first photodetector is centered at around 750 nm, which is approximately a 160 nm shift in comparison with that of the second one (910 nm). What is more, the corresponding photo-absorption ratio (photo-absorption device 2/photo-absorption device 1) increases gradually with increasing wavelength, and approaches nearly 100% at a wavelength of 1100 nm, suggesting very close absorption in the NIR region. A similar finding was also observed in the corresponding photocurrents of both heterojunction photodetectors, leading to a gradual increase in photocurrent ratio with increasing wavelength (Fig. 3(c)). This consistence in photo-absorption and photocurrent is reasonable considering the fact that the majority of the absorbed photons will contribute to the formation of photocurrent, as a consequence of longer carrier diffusion length than the thickness of the thin Si (316 μm *vs.* 20 μm, a detailed calculation of the diffusion length can be found in the ESI†). As a matter of fact, a similar tendency in photocurrent ratios was also observed for other devices composed of thin Si wafers with different thickness (*e.g.* 1, 5, 10 and 40 μm), except for a slight difference in slope and wavelength range. This observation is important as the relationship between the photocurrent ratio and wavelength actually obeys a monotonic function in a certain wavelength range, which makes it possible for us to determine the wavelength of the incident light. But as the thickness of the silicon wafer increases, more light will be absorbed by the first device, and the incident light range that can be detected by the second device is relatively narrow, leading to the narrower detection range of the wavelength detector. However, in the case of small thickness, the photo-absorption of the first device and the second device is similar, which is unfavourable for us to distinguish wavelength by using the photocurrent ratio. Therefore, the Si wafer with a thickness of 20 μm is the best choice, as shown in Fig. 3(d).

Considering the availability and processing cost of thin Si wafers (it is highly challenging to get a uniform Si wafer with thicknesses of 1, 5 and 10 μm), 20 μm thin silicon is selected to assemble this device. As often observed in other Gr/semiconductor heterojunction based photodetectors,[39] the present Gr/thin Si/Gr also displays an obvious photoresponse to incident visible light with good reproducibility. Fig. 4(a) shows the current–voltage (I–V) curves in the dark and under 660 nm light illumination with different light intensities. One can easily see that the Gr/thin Si/Gr heterojunction junction is very sensitive to the 660 nm light. In addition, the photocurrent is found to gradually increase from 0.008 to 0.17 mA when the light intensity increases from 0.075 to 5.1 mW cm^{-2} (Fig. 4(b)). Such photoresponse behavior at bias voltage is obviously related to the separation of photo-generated carriers at forward bias

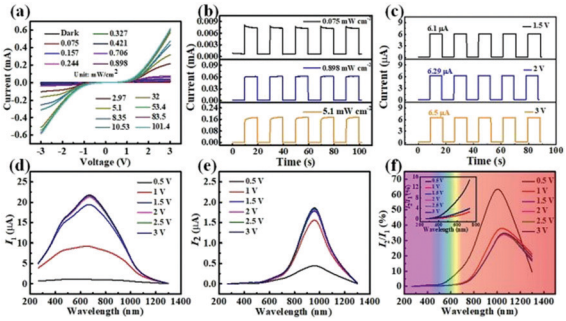

Fig. 4 (a) I–V curves of a single Gr/thin Si/Gr heterojunction photodetector under 660 nm light illumination with different intensities. (b) Photoresponse of the heterojunction photodetector under 660 nm light illumination with different light intensities, at a bias voltage of 2 V. (c) The on/off switching response at various bias voltage, at a light power of 200 μW cm^{-2}. (d) Spectral photoresponse of the first device at different biases. (e) Spectral photoresponse of the second device at different biases. (f) Photocurrent ratio of both devices at different biases, the inset shows the photocurrent ratio for wavelength in the range of 250–700 nm.

voltage, as illustrated by the energy band diagram shown in Fig. S5 (ESI†). During this photoelectric process, since the bias voltage can directly influence the separation efficiency of photo-generated carriers, large positive bias therefore will lead to a relatively large photocurrent (Fig. 4(c)).

The photoresponse property of the current Gr/thin Si/Gr junction is further quantitatively evaluated by calculating the following key device parameters: responsivity (R), specific detectivity (D^*), and external quantum efficiency (EQE, please refer to the ESI† for more about the calculation). Table S1 (ESI†) summarizes the key device parameters of the Gr/thin Si and other Gr/silicon based photodetectors. It is seen that compared with other NIR devices, the current Gr/thin Si has relatively low R, D^* and EQE for a wavelength of 800 nm. The poor photoresponse might be attributed to the usage of a very thin Si wafer, which is unable to absorb sufficient infrared light due to the thin thickness and relatively small absorption coefficient in the NIR range. In addition to the relatively poor device performance, further device analysis reveals that the present thin Si can also bring about a huge change in spectral response. Fig. 4(d) plots the photocurrent of the first device as a function of different wavelengths. One can easily find that the peak sensitivity is located at around 660 nm, which means a 310 nm blue-shift in comparison with conventional Gr/bulk Si heterojunction devices (peak sensitivity at around 970 nm).[40] This photoelectric property is quite different from what was observed in the second device, whose peak sensitivity is very close to that of Gr/bulk Si heterojunction devices. In spite of the huge difference in spectral selectivity, such discrepancy, to our surprise, can allow us to determine the wavelength of incident light by using the photocurrent ratio. Fig. 4(f) shows the photocurrent ratio (I_2/I_1) for the wavelength in the range from 250 to 1050 nm. It is revealed that the I_2/I_1 slowly increases when the wavelength increases from 250 to 700 nm (the inset of Fig. 4(f)), and starts to increase rapidly when the wavelength is in the range from 700 to 1050 nm. Nonetheless, when the

 This journal is © The Royal Society of Chemistry 2021

Published on 27 May 2021. Downloaded by HeFei University of Technology on 8/4/2021 2:17:17 AM.

wavelength further increases from 1050 to 1300 nm, the photocurrent ratio begins to decrease, suggesting the operation region for the present wavelength sensor is 250–1050 nm. In our work, as for the detection of short-wavelength light, the photocurrent of the second device is small and very close to the noise signal, which means that it is nearly impossible for us to quantitatively determine wavelength by using a photocurrent ratio. On the other hand, since the present theory can be applied to other semiconductor materials, which means if other narrow band gap semiconductors with less than 1.0, 0.5, or even 0.2 eV are used, the detection range of the wavelength detector can be extended to the near infrared or mid wavelength infrared light range.

It is worth noting that when bias voltage is set to be 0.5 V, the photocurrents for both photodetectors are relatively smaller than that in other biases. A slight increase in bias voltage from 0.5 to 1.0 V will lead to a substantial increase in photocurrent for both devices. Interestingly, when the bias was further increased to 1.5, 2, 2.5 and even 3 V, a saturation in photocurrent was observed (Fig. 4(d) and (e)). Such an evolution in photocurrent is reasonable as the magnitude of photocurrent for the current metal–semiconductor–metal (M–S–M)-like photodetector is mainly determined by the separation efficiency of both devices, which are directly associated with the bias voltage. The relatively small photocurrent at 0.5 V is due to the poor separation efficiency even though the quantity of photon-induced electron hole pairs (EHPs) is sufficiently large. This difficulty in carrier separation was alleviated when the bias voltage was slightly increased to 1.0 and 1.5 V, leading to an obvious increase in photocurrent. Further increase in bias voltage however can hardly lead to any increase in photocurrent as nearly all the EHPs will be efficiently separated by the bias voltage. This bias voltage dependent photocurrent relationship actually leads to a relatively stable photocurrent ratio in the bias voltage from 1.5 to 3.0 V (Fig. 4(f)), which signifies that the operation bias voltage for the present wavelength sensor should be 1.5 to 3.0 V.

Further device analysis finds that the photocurrents of both devices for all incident light were all increased when the light intensity increased from 200 to 1200 μW cm^{-2} (Fig. 5(a)), due to increased photo-generated carriers at relatively high intensity. However, in the meantime, the spectral selectivity for both devices virtually remains unchanged. Careful examination of the photocurrent ratio at various light intensities in Fig. 5(b) reveals that the relationship between photocurrent ratio and wavelength at an intensity of 200 μW cm^{-2} can actually be described by a strictly monotonic function, as shown in eqn 2:

$$y = 0.0000018 \times e^{\lambda/84.68} + 0.012 \quad (2)$$

where y is the photocurrent ratio, and λ is the wavelength of the incident light. As the light intensity can influence the photocurrent ratio, the strictly monotonic functions corresponding to other various light intensities can also be obtained (see the ESI†). For the sake of convenience, by introducing a new variable p which is the light intensity, the five strictly monotonic

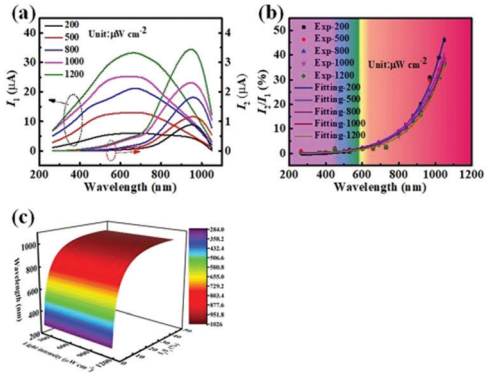

Fig. 5 (a) Photocurrent of both Gr/thin Si/Gr heterojunction devices under various light illuminations with different intensities, at a bias voltage of 2 V. (b) Photocurrent ratio of the second device to the first device under various light illuminations with different intensities, at a bias voltage of 2 V. (c) Diagram of wavelength dependent photocurrent ratios under illumination with various light intensities.

functions can be further re-written as an equation:

$$\lambda = 148.17 + 120.94 \times \left(\frac{p}{8.63\times10^{16}}\right)^{-\frac{\ln\frac{p}{8.63\times10^{16}}}{2\times(-6.16\times10^{14})^2}} + 378.23 \times \left(\frac{y}{0.45}\right)^{-\frac{\ln\frac{y}{0.45}}{11.81}} + 378.25 \times \exp\left\{-\frac{\left(\ln\frac{p}{8.63\times10^{16}}\right)^2}{2\times(-6.16\times10^{14})^2} - \frac{\left(\ln\frac{y}{0.45}\right)^2}{11.81}\right\} \quad (3)$$

By using the above function, the wavelength dependent photocurrent ratio for various light intensities was then plotted. As shown in Fig. 5(c), the relationship for these three variables can actually be numerically described by a curved surface. That means, once the intensity of the incident light and photocurrent ratio are known, the corresponding wavelength can be easily deduced. In order to check the reliability of the present Gr/thin Si/Gr heterojunction device for wavelength detection, the wavelengths obtained by both experimental and numerical calculations were compared (in our experiment, at a certain power intensity, a light source with known wavelength (λ_{exp}) was firstly shone onto the wavelength detector, and the resulting photocurrent ratio was then used to calculate the wavelength (λ_{cal}) through the eqn (3). The deviation of the measurement result from the true value is defined as the RMSE (root-mean-square error) and the relative error). Table 1 analyzes the root-mean-square error and the relative error in the wavelength region from deep ultraviolet light to near infrared light. It can be easily seen that the root-mean-square error is less than 5 nm.[41–43] What is more, the average root-mean-square error is 2.30 nm. Furthermore, the majority of relative errors are less than ±0.7%, except for a relatively high value of ±1.53% in the ultraviolet region. Such a relative error is much

Published on 27 May 2021. Downloaded by HeFei University of Technology on 8/4/2021 2:17:17 AM.

Table 1 Error analysis of experimental and theoretical data

P (μW cm^{-2})	I_2/I_1	λ_{cal} (nm)	λ_{exp} (nm)	RMSE (nm)	Relative error (%)
200	0.00000010	269.11	265	4.11	−1.53
200	0.0033	366.76	365	1.76	−0.48
500	0.0033	364.43	365	0.57	+0.16
500	0.0072	446.93	450	3.07	+0.69
800	0.0075	452.06	450	2.06	−0.46
800	0.013	530.23	530	0.23	−0.044
1000	0.028	662.84	660	2.84	−0.43
1000	0.040	729.76	730	0.24	+0.033

better than previous studies.[44,45] This superior wavelength detection performance suggests the present device may find potential application in other optoelectronic devices and systems. Furthermore, for nearly all semiconductor materials, their penetration depths are dependent on the incident wavelength. Thereby by replacing the silicon with other semiconducting materials, it is possible to achieve other wavelength sensors with different detection ranges.

Conclusions

To summarize, we have developed a wavelength detector based on two vertical stacking Gr/thin Si/Gr heterojunctions. Theoretical simulation from TCAD shows that the two neighboring devices exhibit sharp contrast in photo-absorption and photo-absorption rate for both devices when light illumination with different wavelengths penetrates them. Such unique optical properties are due to the thin thickness of the Si wafer and the wavelength dependent absorption coefficient. It is also revealed that the spectral response of both devices is highly dependent on the wavelength of incident light, which leads to a huge difference in photocurrent for the two Gr/thin Si/Gr heterojunctions. Such a wavelength dependent photocurrent for both devices can facilitate the precise detection of the light wavelength as the relationship between the photocurrent ratio of both devices, the wavelength and intensity of incident light can be described by an equation. Further device analysis determines that the present wavelength sensor can readily detect the wavelength in the range from 250–1050 nm, with an average root-mean-square error of 2.30 nm and a relative error less than $\pm$1.5%, which is much better than previously reported devices. We believe such a new concept of wavelength detector may find potential application in future integrated devices.

Author contributions

L. L. conceived the idea. L. W. performed the simulation. T. F. prepared the device fabrication, and wrote the manuscript. C. X. analyzed the data from a theoretical perspective. D. W. and F. L. advised on device optimization. All the authors discussed the results, and commented on the paper.

Conflicts of interest

There are no conflicts to declare.

Acknowledgements

The authors thank Dr Mei Yao from the School of Mathematics of HFUT for her helpful discussion. This work was supported by the National Natural Science Foundation of China (NSFC, No. 62074048), the Fundamental Research Funds for the Central Universities (JZ2018HGXC0001), and the Open Foundation of Anhui Provincial Key Laboratory of Advanced Functional Materials and Devices (4500-411104/011).

Notes and references

1 J. Mcdowell, *IEEE Potentials*, 2008, **27**, 34–39.
2 R. D. Jansen-van Vuuren, A. Armin, A. K. Pandey, P. L. Burn and P. Meredith, *Adv. Mater.*, 2016, **28**, 4766–4802.
3 W. D. Hu, Z. H. Ye, L. Liao, H. L. Chen, L. Chen, R. J. Ding, L. He, X. S. Chen and W. Lu, *Opt. Lett.*, 2014, **39**, 5130–5133.
4 Z. Y. Yang, T. Albrow-Owen, H. X. Cui, J. Alexander-Webber, F. X. Gu, X. M. Wang, T. C. Wu, M. H. Zhuge, C. Williams, P. Wang, A. V. Zayats, W. W. Cai, L. Dai, S. Hofmann, M. Overend, L. M. Tong, Q. Yang, Z. P. Sun and T. Hasan, *Science*, 2019, **365**, 1017–1020.
5 X. X. Zhu, L. H. Bian, H. Fu, L. X. Wang, B. S. Zou, Q. H. Dai, J. Zhang and H. Z. Zhong, *Light: Sci. Appl.*, 2020, **9**, 1–9.
6 M. N. Zhang, X. H. Wu, A. Riaud, X. L. Wang, F. X. Xie, W. J. Liu, Y. F. Mei, D. W. Zhang and S. J. Ding, *Light: Sci. Appl.*, 2020, **9**, 1–13.
7 W. L. Tsai, C. Y. Chen, Y. T. Wen, L. Yang, Y. L. Cheng and H. W. Lin, *Adv. Mater.*, 2019, **31**, 1900231.
8 T. K. Woodstock and R. F. Karlicek, *IEEE Sens. J.*, 2020, **20**, 12364–12373.
9 G. Goos and J. Hartmanis, *Lecture Notes in Computer Science*, Springer, 1985.
10 J. H. Han, D. H. Kim, T. W. Lee, Y. M. Jeon, H. S. Lee and K. C. Choi, *ACS Photonics*, 2018, **5**, 3322–3330.
11 Y. J. Jung and N. Park, *J. Opt. Soc. Korea*, 2016, **20**, 180–187.
12 H. X. Sun, W. Tian, X. F. Wang, K. M. Deng, J. Xiong and L. Li, *Adv. Mater.*, 2020, **32**, 1908108.
13 T. Xu, Y. K. Wu, X. G. Luo and L. J. Guo, *Nat. Commun.*, 2010, **1**, 1–5.
14 T. Hirano, N. Shimatani, K. Kintaka, K. Nishio, Y. Awatsuji and S. Ura, *Jpn. J. Appl. Phys.*, 2014, **53**, 032501.
15 P. B. Catrysse and B. A. Wandell, *J. Opt. Soc. Am. A*, 2003, **20**, 2293–2306.
16 G. Langfelder, F. Zaraga, A. Longoni and C. Buffa, *IEEE Sens. J.*, 2011, **11**, 1979–1986.
17 A. Longoni, F. Zaraga, G. Langfelder and L. Bombelli, *IEEE Electron Device Lett.*, 2008, **29**, 1306–1308.
18 M. A. Martínez, E. M. Valero, J. Hernández-Andrés, J. Romero and G. Langfelder, *Appl. Opt.*, 2014, **53**, C14–C24.
19 S. Feruglio, G. N. Lu, P. Garda and G. Vasilescu, *Sensors*, 2008, **8**, 6566–6594.

 This journal is © The Royal Society of Chemistry 2021

Published on 27 May 2021. Downloaded by HeFei University of Technology on 8/4/2021 2:17:17 AM.

20 C. Richard, T. Courcier, P. Pittet, S. Martel, L. Ouellet, G. N. Lu, V. Aimez and P. G. Charette, *Opt. Express*, 2012, **20**, 2053–2061.
21 X. Y. Fang, V. S. Hsiao, V. P. Chodavarapu, A. H. Titus and A. N. Cartwright, *IEEE Sens. J.*, 2006, **6**, 661–667.
22 G. Sharma, *Digital Color Imaging Handbook*. CRC press, America, 2017.
23 K. M. Findlater, D. Renshaw, J. E. D. Hurwitz, R. K. Henderson, T. E. R. Bailey, S. G. Smith, M. D. Purcell and J. M. Raynor, IEEE, Workshop on CCDs, *IEEE Electron Devices Soc.*, 2001, 60–63.
24 D. Knipp, R. A. Street, H. Stiebig, M. Krause, J. P. Lu, S. Ready and J. Ho, *Sens. Actuators, A*, 2006, **128**, 333–338.
25 W. Qarony, M. Kozawa, H. A. Khan, M. I. Hossain, A. Salleo, Y. H. Tsang, J. Y. Hardeberg, H. Fujiwara and D. Knipp, *Adv. Mater. Interfaces*, 2020, 2000459.
26 Y. H. Gu, L. Zhang, J. K. W. Yang, S. P. Yeoa and C. W. Qiu, *Nanoscale*, 2015, **7**, 6409–6419.
27 M. I. Hossain, H. A. Khan, M. Kozawa, W. Qarony, A. Salleo, J. Y. Hardeberg, H. Fujiwara, Y. H. Tsang and D. Knipp, *ACS Appl. Mater. Interfaces*, 2020, **12**, 47831–47839.
28 A. M. Hoang, A. Dehzangi, S. Adhikary and M. Razeghi, *Sci. Rep.*, 2016, **6**, 24144.
29 L. B. Luo, H. Hu, X. H. Wang, R. Lu, Y. F. Zou, Y. Q. Yu and F. X. Liang, *J. Mater. Chem. C*, 2015, **3**, 4723–4728.
30 X. M. Li, D. Xie, H. Park, T. Y. Helen Zeng, K. L. Wang, J. Q. Wei, M. L. Zhong, D. H. Wu, J. Kong and H. W. Zhu, *Adv. Energy Mater.*, 2013, **3**, 1029–1034.
31 Y. L. Xu, X. Wei, C. Wang, J. Cao, Y. G. Chen, Z. Q. Ma and Y. You, *Sci. Rep.*, 2017, **7**, 45392.
32 G. H. Han, F. Güne, J. J. Bae, E. S. Kim, S. J. Chae, H. J. Shin, J. Y. Choi, D. Pribat and Y. H. Lee, *Nano Lett.*, 2011, **11**, 4144–4148.
33 C. Xie, Y. Wang, Z. X. Zhang, D. Wang and L. B. Luo, *Nano Today*, 2018, **19**, 41–83.
34 F. X. Liang, Y. Gao, C. Xie, X. W. Tong, Z. J. Li and L. B. Luo, *J. Mater. Chem. C*, 2018, **6**, 3815–3833.
35 Z. H. Sun and H. X. Chang, *ACS Nano*, 2014, **8**, 4133–4156.
36 L. Wang, H. H. Luo, H. H. Zuo, J. Q. Tao, Y. Q. Yu, X. P. Yang, M. L. Wang, J. G. Hu, C. Xie, D. Wu and L. B. Luo, *IEEE Trans. Electron Devices*, 2020, **67**, 3211–3214.
37 Y. W. Kuang, Y. S. Liu, Y. L. Ma, J. Xu, X. F. Yang and J. F. Feng, *Int. Soc. Opt. Photonics*, 2015, **9656**, 96560.
38 N. M. Miskovsky, P. H. Cutler, A. Mayer, B. L. Weiss, B. Willis, T. E. Sullivan and P. B. Lerner, *J. Nanotechnol.*, 2012, **2012**, 512379.
39 K. Huang, X. G. Yu, J. K. Cong and D. R. Yang, *Adv. Mater. Interfaces*, 2018, **5**, 1801520.
40 P. F. Wang, Y. Liu, J. Yin, W. Y. Ma, Z. M. Dong, W. Zhang, J. L. Zhu and J. L. Sun, *J. Mater. Chem. C*, 2019, **7**, 887–896.
41 S. Schidl, A. Polzer and H. Zimmermann, *Electron. Lett.*, 2012, **48**, 1489–1490.
42 G. N. Lu, M. B. Chouikha, G. Sou and M. Sedjil, *Electron. Lett.*, 1996, **32**, 594–596.
43 N. Tadić, S. Schidl and H. Zimmermann, *Opt. Lett.*, 2014, **39**, 5042–5045.
44 A. Polzer, W. Gaberl and H. Zimmermann, *Electron. Lett.*, 2011, **47**, 614–615.
45 A. Polzer, W. Gaberl, M. Davidovic and H. Zimmermann, *IEEE*, 2011, 1937–1940.